Magnetic Resonance in Medicine

Prostate DCE-MRI with B_1^+ correction using an approximated analytical approach

Xinran Zhong[1,2] | Thomas Martin[1,2] | Holden H. Wu[1,2] (iD) | Krishna S. Nayak[3] |
Kyunghyun Sung[1,2]

[1] Department of Radiological Sciences, David Geffen School of Medicine, University of California, Los Angeles, California

[2] Physics and Biology in Medicine Graduate Program, David Geffen School of Medicine, University of California, Los Angeles, California

[3] Ming Hsieh Department of Electrical Engineering, University of Southern California, Los Angeles, California

Correspondence
Xinran Zhong, Department of
Radiological Sciences, David Geffen
School of Medicine, 300 UCLA Medical
Plaza, Suite B114 Los Angeles, CA
90095
Email: XZhong@mednet.ucla.edu

Purpose: To develop and evaluate a practical B_1^+ correction method for prostate dynamic contrast-enhanced (DCE) MRI analysis.

Theory: We proposed a simple analytical B_1^+ correction method using a Taylor series approximation to the steady-state spoiled gradient echo signal equation. This approach only requires B_1^+ maps and uncorrected pharmacokinetic (PK) parameters as input to estimate the corrected PK parameters.

Methods: The proposed method was evaluated using a prostate digital reference object (DRO), and 82 in vivo prostate DCE-MRI cases. The approximated analytical correction was compared with the ground truth PK parameters in simulation, and compared with the reference numerical correction in in vivo experiments, using percentage error as the metric.

Results: The prostate DRO results showed that our approximated analytical approach provided residual error less than 0.4% for both K^{trans} and v_e, compared to the ground truth. This noise-free residual error was smaller than the noise-induced error using the reference numerical correction, which had a minimum error of 2.1+4.3% with baseline signal-to-noise ratio of 234.5. For the 82 in vivo cases, K^{trans} and v_e percentage error compared to the reference numerical correction method had a mean of 0.1% (95% central range of [0.0%, 0.2%]) across the prostate volume.

Conclusion: The approximated analytical B_1^+ correction method provides comparable results with less than 0.2% error within 95% central range, compared to reference numerical B_1^+ correction. The proposed method is a practical solution for B_1^+ correction in prostate DCE-MRI because of its simple implementation.

KEYWORDS
DCE-MRI, B_1^+ correction, prostate, pharmacokinetic modeling, quantitative analysis

1 | INTRODUCTION

Prostate cancer is one of the leading causes of cancer deaths for men in the United States.[1] Biopsy is one of the current gold standards for diagnosing prostate cancer; however, it is invasive and has a relatively low specificity.[2]

Multiparametric MRI, which includes dynamic contrast-enhanced MRI (DCE-MRI), is now widely used as a promising noninvasive technique for diagnosing prostate cancer.[3-5] Conventional image analyses for DCE-MRI are typically based on qualitative analyses of signal uptake, where the subjective evaluation or qualitative analyses are

limited by interobserver variability and high dependence on data acquisition.[6]

Quantitative DCE-MRI has shown great potential in tumor detection, staging, and treatment response evaluation.[7-9] Quantitative analysis of DCE-MRI usually requires modeling to generate contrast concentration curves in the tissue and then uses pharmacokinetic (PK) analysis to estimate parameters such as volume transfer constant (K^{trans}) and extravascular extracellular volume fraction (v_e).[10] To calculate an accurate contrast agent concentration curve, precontrast T_1 (T_{10}) maps need to be estimated. A variable flip angle (VFA) method is commonly used for T_{10} estimation.[11,12] However, the VFA image acquisition is sensitive to flip angle variation caused by transmit radiofrequency (B_1^+) field inhomogeneity.[13-15]

Increased signal-to-noise ratio (SNR) from 3 Tesla (T) MRI systems can improve the quantification accuracy, thus becoming preferable for prostate multiparametric MRI.[16] However, B_1^+ field inhomogeneity becomes more severe with increased field strengths ($\geq 3.0T$).[17] If B_1^+ field is inhomogeneous, the spins within excitation can fail to achieve the exact flip angle as prescribed, thus reducing the accuracy of the quantitative analysis of DCE-MRI. Previous studies have shown an intersubject B_1^+ variation of 32% in the prostate[18] at 3T, which can induce significant errors into the PK estimation. Di Giovanni et al. showed that the 55% overestimation of flip angle attributed to B_1^+ inhomogeneity could result in up to 66% underestimation for measured K^{trans} and 77% underestimation of v_e.[19]

Various B_1^+ mapping techniques have been developed to enable B_1^+ compensation, including the double-angle method,[20] Block-Siegert,[21] actual flip angle imaging,[22] and reference region VFA.[23] However, even if B_1^+ maps are available, applying the B_1^+ correction to quantitative DCE-MRI analysis is sometimes difficult because of practical limitations when closed-form software is used. Using B_1^+-corrected flip angles, the B_1^+ correction requires a full numerical reprocessing of the entire DCE-MRI modeling, from signal intensity to PK parameters. This numerical reprocessing can be challenging especially when closed-source software is used for DCE-MRI analysis[24] and can be time-consuming because of the pixel-by-pixel reprocessing. Especially for clinical or clinical research settings, simple yet efficient B_1^+ correction approaches will be highly desirable because closed-form or commercial software is commonly used.

In this work, we present a simplified and practical approach that compensates for B_1^+ inhomogeneity in quantitative prostate DCE-MRI analysis. Our proposed approximated analytical approach enables a simple and practical application of B_1^+ correction in quantitative DCE-MRI because it does not require full access to the entire DCE-MRI analysis and avoids repeated pixel-by-pixel PK parameter estimation. The accuracy of the approximated analytical approach was evaluated using numerical simulation and prostate-specific digital reference object (DRO). The approximated analytical approach was also compared with reference numerical correction[24] on 82 in vivo 3T prostate DCE-MRI cases.

2 | THEORY

2.1 | Quantitative analysis for prostate DCE-MRI

The radiofrequency-spoiled gradient echo sequence is used to acquire images for DCE-MRI and to obtain pre-contrast T_1 (T_{10}) map. The signal intensity (S) of radiofrequency-spoiled gradient echo, ignoring T_2^* decay, can be expressed as:

$$S = M_0 \frac{\sin\theta(1-E_1)}{1-E_1\cos\theta} \tag{1}$$

where M_0 is the equilibrium magnetization, θ is the flip angle, and $E_1 = e^{-TR/T_1}$.

VFA with radiofrequency-spoiled gradient echo can be used to generate T_{10} maps by using a set of flip angles, $\alpha_i \in \{\alpha_1, \alpha_2, \cdots, \alpha_N\}$, with fixed repetition time (TR) and echo time (TE).[11,12] T_{10} can be calculated using a simple linear regression by substituting α_i and $E_{10} = e^{-TR/T_{10}}$ into Equation 1 (Eq. 2):

$$\frac{S(\alpha_i)}{\sin(\alpha_i)} = E_{10} \frac{S(\alpha_i)}{\tan(\alpha_i)} + M_0(1-E_{10}) \tag{2}$$

Once T_{10} is estimated, the dynamic T_1 map, $T_1(t)$, generated by using radiofrequency-spoiled gradient echo sequence with the flip angle β, can be computed by using T_{10} and the normalized signal intensity $S(T_1(t))/S(T_{10})$, where $S(T_{10})$ is the precontrast baseline signal intensity and $S(T_1(t))$ is the DCE signal intensity, as shown in Equation 3:

$$\Xi = \frac{S\left(T_1(t)\right) - S(T_{10})}{S(T_{10})} = \frac{\left(E_1(t) - E_{1,0}\right)(\cos\beta - 1)}{(E_{1,0} - 1)\left(E_1(t)\cos\beta - 1\right)} \tag{3}$$

To determine the PK parameters, the tissue contrast agent concentration, C(t), needs to be calculated from $T_1(t)$ and T_{10}. C(t) is proportional to the change of longitudinal relaxation rate and can be computed by (Eq. 4):

$$C(t) = \frac{1}{r_1}\left(\frac{1}{T_1(t)} - \frac{1}{T_{10}}\right) \tag{4}$$

where r_1 is the T_1 relaxivity related to the contrast agent. Once C(t) is estimated, PK modeling such as standard Tofts model[25] can be applied to estimate PK parameters (K^{trans} and v_e) using nonlinear curve fitting:

$$C(t) = K^{trans} \int_0^t C_p(\tau)e^{-\frac{K^{trans}}{v_e}(t-\tau)}d\tau \tag{5}$$

where $C_p(t)$ is the contrast agent concentrations in the plasma (or arterial input function [AIF]), K^{trans} is the rate constant

from plasma to extravascular-extracellular space, and v_e is the fractional volume constant of the extravascular-extracellular space. $C_p(t)$ can be either measured or preassumed.[6]

When there exists B_1^+ inhomogeneity, the prescribed flip angles (α_i and β) are not the same as the actual flip angle, which causes errors in the measurement of PK parameters. B_1^+ estimation is needed to accurately determine α_i and β for each pixel.

2.2 | B_1^+ correction: reference numerical approach

The conventional approach that compensates for B_1^+ inhomogeneity numerically reprocesses the whole quantitative DCE-MRI analysis with B_1^+-corrected flip angles.[24] For a given B_1^+ mapping technique, a pixel-by-pixel relative flip angle (defined as $k = \frac{\alpha_i\prime}{\alpha_i} = \frac{\beta\prime}{\beta}$, where α_i and β are the prescribed flip angles, and α_i' and β' are the actual flip angles), is determined. The B_1^+-corrected flip angle, assumed to be the actual flip angle, can be simply computed by multiplying k and the prescribed flip angle. The whole DCE-MRI analysis needs to be reprocessed for each pixel using the B_1^+-corrected flip angles. As a note, all variables with prime (') indicate B_1^+-corrected variables. When α_i' is determined, then it is used in Equation 2 to estimate T_{10}', and β' has to be used in Equation 3 to estimate T_1'(t). Once T_{10}' and T_1'(t) are computed, both K^{trans}' and v_e' can be computed by $C'(t)$ from Equations 4 and 5.[24]

This numerical approach is well defined, but can be demanding because it requires full access to the MRI modeling, PK modeling, and raw DCE-MRI images. Many commercial and closed-source software do not include pixel-by-pixel B_1^+ correction, nor can we modify the software to perform B_1^+ correction with the numerical approach. Moreover, even when the numerical approach is possible, the B_1^+ correction would need to repeat the pixel-by-pixel estimation of PK parameters, which can be time-consuming, especially for volumetric PK maps.

2.3 | B_1^+ correction: approximated analytical approach

An analytical approach is desirable in many clinical and research settings because it allows direct derivation of B_1^+-corrected PK parameters. Analytical correction does not require full access to the DCE modeling, nor raw DCE-MRI images, and can enable a more practical B_1^+ correction process by only using B_1^+ maps and uncorrected PK maps as input. However, the full analytical expression of the B_1^+-corrected PK parameters is highly complicated to derive because of multiple nonlinear processes, as described before in Equations 2 to 5. Here, we describe an approximated analytical approach to derive B_1^+-corrected PK parameters (K^{trans}' and v_e') by approximating the full analytical expression with

certain assumptions. This approximated analytical approach will improve the utility of B_1^+ correction in DCE-MRI in various settings with minimal approximation error.[26]

In the approximated analytical approach, we assume that the flip angles and TR/T_1 are small ($\alpha_i^3 \approx 0$, $\beta \approx 0$, TR/$T_{10} \approx 0$, and TR/$T_1(t) \approx 0$), and k is close to 1 (k $\approx$ 1). Using a Taylor series approximation on Equations 2 and 3, T_{10}' and T_1'(t) can be simply expressed as $T'_{10} \approx \frac{1}{k^2} T_{10}$ and $T'_1(t) \approx \frac{1}{k^2} T_1(t)$. For simplicity, we used two flip angles for the VFA process in the analytical derivation. Based on Equation 4, the corrected contrast agent concentration curve $C'(t) = k^2 C(t)$ can be derived. As a result, the B_1^+-corrected PK parameters can be approximated as $K^{trans}\prime \approx k^2 K^{trans}$ and $v'_e \approx k^2 v_e$ from Equation 5. The full derivation of the approximated approach can be found in the Appendix. Using the approximated derivation of B_1^+-corrected PK parameters from uncorrected PK parameters allows for direct compensation for B_1^+ inhomogeneity without fully accessing MRI modeling and PK modeling because the relationship does not change regardless of corrected T_{10}, K^{trans} and v_e value.

3 | METHODS

Our approximated analytical approach relies on a set of assumptions, including small flip angles, small TR/T_1, and k close to 1. We first evaluated the approximation by numerical simulation and DRO and then compared the approximated analytical approach with the conventional numerical correction using 82 in vivo prostate DCE-MRI cases based on our standard clinical prostate DCE-MRI protocol.

3.1 | Prostate DRO

We used the numerical simulation and prostate DRO[27-29] to carefully separate each source of errors (e.g., noise and B_1^+ inhomogeneity), providing a more systematic way to evaluate B_1^+ correction approaches. The DRO was composed of simulated grid-based MRI images with a set of preassumed PK parameters, including VFA images as well as dynamic images. We assumed a certain set of PK parameters, K^{trans} (ranged from 0.01 to 0.35 min^{-1}) and v_e (ranged from 0.01 to 0.5), defined as a ground truth set P_{nat}, and generated C(t) based on the set. The detailed sequence parameters are shown in Table 1 and are derived from our clinical prostate DCE-MRI protocol. We then created signals in both VFA images and dynamic T_1-weighted images based on actual flip angles. The B_1^+-induced uncorrected flip angles were created by applying various k (ranged from 0.7 to 1.3) to the actual flip angle, and these uncorrected flip angles were used in the following model fitting from signal intensity to PK parameters (Eqs. 2-5). The calculated parameters were defined as uncorrected parameters P_{uncor}. Both the numerical

TABLE 1 Details of the DRO modification

	QIBA DRO	Prostate DRO
K^{trans}	0.01, 0.02, 0.05, 0.1, 0.2, 0.35 min^{-1}	
v_e	0.01, 0.05, 0.1, 0.2, 0.5	
Relative B_1^+ (k = θ'/θ)	1.2	
T_{10}	1,000 ms	
VFA flip angle	3, 6, 9, 15, 24, 35°	2, 5, 10, 15°
Dynamic flip angle	25°	12°
Repetition time	5 ms	4.17 ms
Patch size	10 × 10 pixels	2 × 2 pixels

and approximated analytical correction methods were applied on the simulated signals to generate the corrected parameters ($P_{cor,N}$ and $P_{cor,A}$).

All signal simulations and fittings were done using Matlab (The Mathworks, Inc., Natick, MA), and the trust-region reflective algorithm[30] with lower bound of zero for K^{trans} and v_e was used in the nonlinear fitting process in PK modeling. In the following analysis, the percentage error relative to ground truth, P_{nat}, was calculated as the evaluation metric. The B_1^+-induced error ($E_{B1, DRO}$) was defined as $\frac{|P_{uncor} - P_{nat}|}{P_{nat}} \times 100\%$ and the correction residual errors for $P_{cor,N}$ and $P_{cor,A}$ were defined by $E_{N, DRO} = \frac{|P_{cor,N} - P_{nat}|}{P_{nat}} \times 100\%$ and $E_{A, DRO} = \frac{|P_{cor,A} - P_{nat}|}{P_{nat}} \times 100\%$.

To assess the bias and variance of the percentage errors for B_1^+ correction under a certain prostate-like DCE-MRI conditions, we first calculated B_1^+-induced and correction residual errors within a realistic range for B_1^+ inhomogeneity in the prostate.[18] The numerical simulation included 100 points with uniformly distributed k between 0.7 and 1.3 for 1 representative combination of $K^{trans} = 0.05$ min^{-1}, $v_e = 0.1$, and $T_{10} = 1,000$ ms. To further assess the B_1^+-induced errors with various K^{trans} and v_e, we created a prostate DRO, modified from the original DRO by Quantitative Imaging Biomarkers Alliance (QIBA),[31] using our clinical prostate DCE-MRI parameters (see Table 1). Other parameters of the prostate DRO are shown in Table 1. The DRO simulation, shown in Figure 1a, was repeated by using three different widely used population-based AIFs[32] (Parker,[33] Weinmann,[34] and Fritz-Hansen[35]) with the standard Tofts model.

Noise was added to both VFA images and dynamic images by $S' = \sqrt{(S+n_1)^2 + n_2^2}$, where S is the original signal intensity and n_1 and n_2 are Gaussian noise with the mean 0 and standard deviation ranging from 5 to 150, resulting in a baseline SNR ranging from 7.8 to 234.5. PK maps with and without correction were calculated as shown in Figure 1b. With each SNR, the process was repeated 25 times, resulting in 100 available samples for each K^{trans} and v_e combination. For fair comparison, estimation parameters (K^{trans} or v_e) larger than 1 were excluded as outliers.[36] $E_{N,DRO}$ and $E_{A,DRO}$ for each SNR from 3,000 pixels (5 × 6 × 100), except for those outliers, were averaged to evaluate residual errors
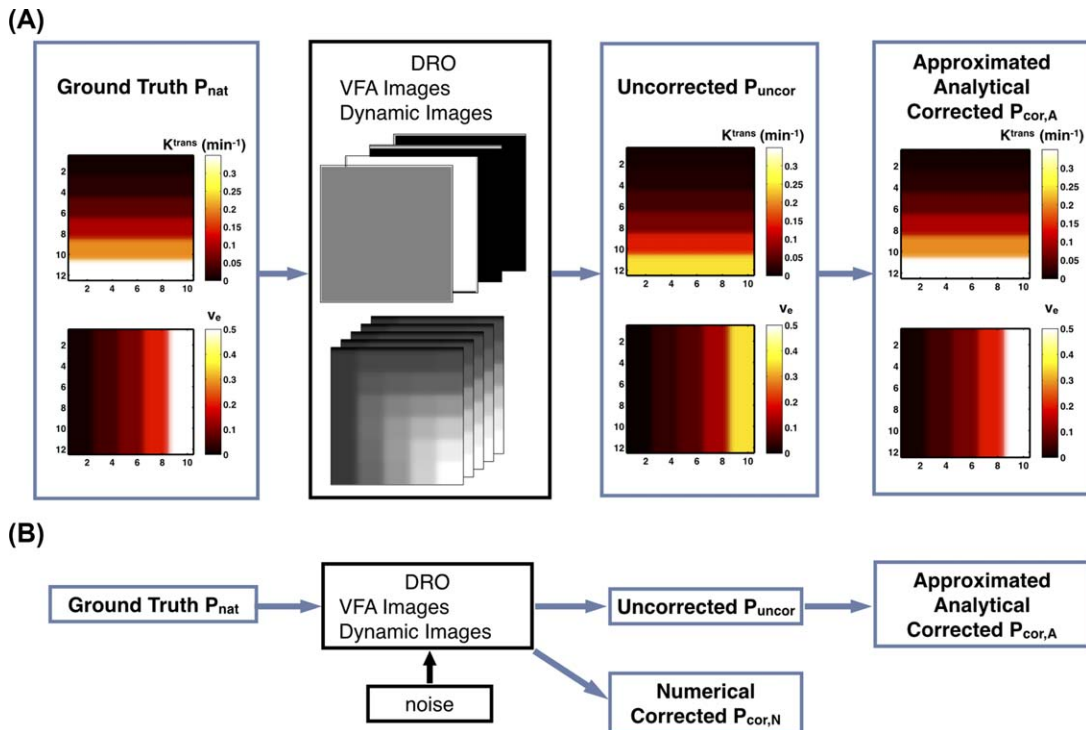
FIGURE 1 Summary of the simulation study design using DRO under various population-averaged AIFs (a) and Gaussian noise (b). The images in (a) are examples of corresponding K^{trans} and v_e maps in each step and DRO images. P represents PK parameters K^{trans} and v_e.
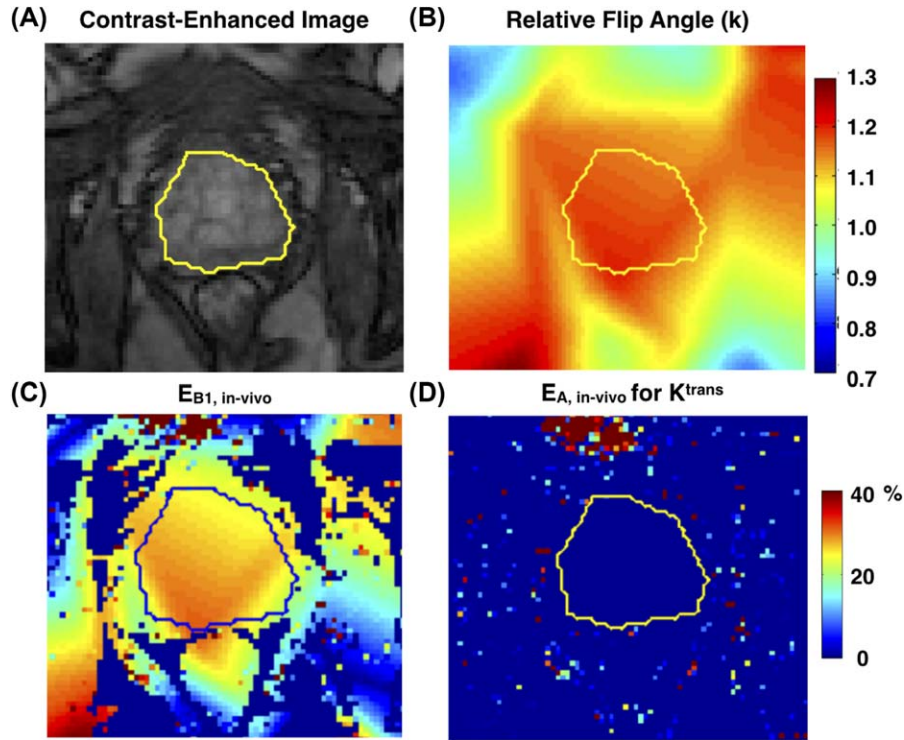
FIGURE 2 A representative slice of ROI positioning for in vivo prostate data. ROI was first drawn on contrast-enhanced images (a) and was copied to corresponding relative B_1^+ (k) map (b) $E_{B1,in-vivo}$ map (c) as well as $E_{A,in-vivo}$ for K^{trans}.

varying with SNRs. Here, $E_{N,DRO}$ provided an estimation of the error tolerance attributed to noise, compared with the approximation-induced error ($E_{A,DRO}$ without noise). Moreover, $E_{N,DRO}$ and $E_{A,DRO}$ for each parameter combination were averaged separately to show the correction residual error distribution with P_{nat}. Linear regression and Bland-Altman plots were used to evaluate the correlation between PK parameters corrected by the 2 correction methods.

Similarly, to test the sensitivity of the 2 correction methods for k variation, we performed Monte-Carlo simulation with random Gaussian noise (0 mean and standard deviation ranging from 0.001 to 0.1) added in ground truth k = 1.2. The sensitivity was evaluated using $E_{A,DRO}$ and $E_{N,DRO}$.

3.2 | In vivo prostate DCE-MRI data

With the local institutional review board approval, 82 cases were used to evaluate the approximated analytical approach in vivo. The 82 cases were acquired between June 2010 and September 2014 (age = 65.9 ± 6.9 years and mass = 81.9 ± 13.5 kg). All in vivo DCE-MRI cases were performed on two 3T scanners (MAGNETOM Skyra and MAGNETOM Trio; Siemens Medical Systems, Erlangen, Germany), using a body array matrix and spine array coil. The 3D SPGR sequence was used in both VFA and dynamic imaging with a TR of 4.17 ms. The slice thickness was 3.6 mm, and the flip angles used were 2, 5, 10, and 15° for variable flip angle acquisition and 12° for dynamic acquisition. For most cases,

a matrix size of 160×160 with 20 slices was used, and those parameters varied slightly for other cases. For VFA imaging, a dual-echo bipolar readout (TE_1 = 1.23 ms; TE_2 = 2.46 ms) was used to generate the fat-only and water-only images using a 2-point Dixon algorithm,[37] and the B_1^+ maps were estimated using reference region VFA.[18] A single-dose injection of gadopentetate dimeglumine (Magnevist; Bayer, Wayne, NJ) contrast agent was administered to the patients at a dose of 0.1 mmol/kg through a peripheral vein at a rate of 2 mL/sec using a mechanical injector, and dynamic images were acquired before, during, and after contrast injection. Approximately 65 contrast-enhanced sets of images (temporal resolution of 4.3 seconds) were acquired sequentially without delay between acquisitions with the total acquisition time of 5 minutes.

The standard Tofts model with Parker AIF[33] was used for the PK modeling. The fitting algorithm and constraint are the same as in DRO experiments. Prostate regions of interest (ROIs) were manually drawn on the 5 central slices in the contrast-enhanced images and were copied to other images such as B_1^+, B_1^+-corrected, and uncorrected PK maps. A representative example of the prostate ROI is shown in Figure 2. The evaluation was performed using percentage error with respect to the B_1^+-corrected parameters using the numerical approach. Specifically, the B_1^+-induced error ($E_{B1, in-vivo}$) was defined by $\frac{|P_{uncorr}-P_{cor,N}|}{P_{cor,N}} \times 100\%$, and the correction residual error ($E_{A, in-vivo}$) was defined by $\frac{|P_{cor,A}-P_{cor,N}|}{P_{cor,N}} \times 100\%$. The mean, standard deviation, and 95% central range of all the
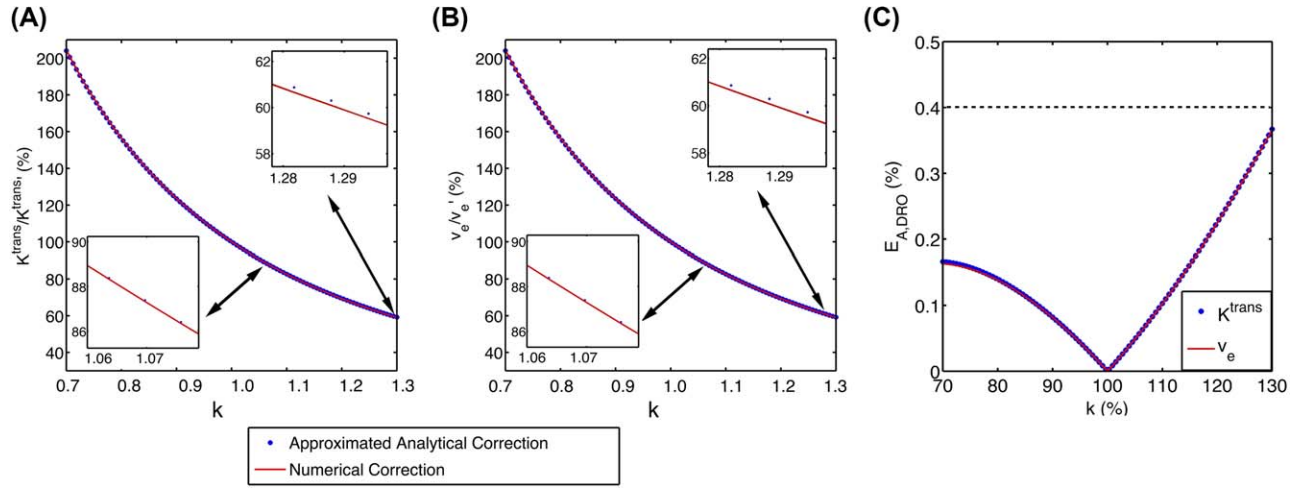
FIGURE 3 Comparison between numerical correction method and approximated analytical correction method in simulation with k ranging from 0.7 to 1.3 (ground truth $K^{trans'} = 0.05\ min^{-1}$, $v_e = 0.1$, and $T_{10} = 1{,}000\ ms$) for K^{trans} (a) and v_e (b) and $E_{A,DRO}$ for K^{trans} and v_e (c). Two example areas around k of 1.1 and 1.3 are zoomed. The difference between blue and red curves indicates $E_{A,DRO}$ (also shown in [c]), and the difference of y-axis and 100% indicates $E_{B1,DRO}$. $E_{A,DRO}$ is negligible compared to $E_{B1,DRO}$.

voxels within the ROIs from all 82 patients were computed. An average k and the residual error for each patient's volumetric ROI from 5 central slices were also computed to evaluate the approximated analytical method among different cases. Any pixels with estimated v_e or K^{trans} larger than 1 were considered to be outliers[36] and therefore were excluded for all in vivo experiments.

4 | RESULTS

4.1 | Prostate DRO

Figure 3 shows that the numerical and approximated analytical methods are comparable in the numerical simulation with k variation. Within k range of 0.7 to 1.3, the maximum $E_{A,DRO}$ is less than 0.4% for K^{trans} and v_e (Fig. 3c). This is negligible compared to $E_{B1,DRO}$ (maximum of 104.1%). Figure 3 also describes how P_{uncor} deviates from the ground truth as k varies. For example, when k equals to 1.28, uncorrected K^{trans} and v_e underestimate around 40% of the true value. For all simulated points, $P_{cor,N}$ and P_{nat} are the same with a precision of 10^{-12} as expected, assuring the accuracy of the numerical correction method.

Despite K^{trans} and v_e variation, the $E_{A,DRO}$ is small and uniform for K^{trans} and v_e for all three AIFs based on the DRO simulation with a k of 1.2 (Supporting Information Figure S1). The maximum $E_{A,DRO}$ is 0.2% for K^{trans} estimation and 0.4% for v_e estimation, whereas the $E_{B1,DRO}$ of $30.7 \pm 0.1\%$. Overall, $E_{A,DRO}$ is almost negligible compared to $E_{B1,DRO}$ regardless of P_{nat} and the preassumed AIFs. By comparison, $E_{N,DRO}$ has a maximum of 0.2%. This further confirms the accuracy of the numerical correction method under the noise-free situation. These results are consistent with our expectation in the Theory section.

With various levels of noise added in DRO, a minimum $E_{N,DRO}$ of $2.1 \pm 4.3\%$ with baseline SNR of 234.5 was observed, which indicates the estimation uncertainty induced by noise. Based on previous simulation, the maximum $E_{A,DRO}$ without noise is 0.4%, which is much smaller than the minimum $E_{N,DRO}$ induced by minimal noise of standard deviation of 5. The overall residual errors against baseline SNR are shown in Figure 4. Across various baseline SNRs (ranging from 7.8 to 234.5), the difference between $E_{N,DRO}$ and $E_{A,DRO}$ is minimal compared to $E_{N,DRO}$, which means that the approximation-induced error is small compared to noise-induced error. For example, when baseline SNR is 41.2, the noise-induced error for the numerical correction method is 21.9% for K^{trans} and 14.4% for v_e. However, the difference of the mean error of the analytical correction method from mean error of numerical correction method is 4.3% for K^{trans} and –0.1% for v_e. Those results indicate that under various noise levels, the analytical correction method provides similar performance as the numerical correction method.

More specifically, with an example baseline SNR of 38.5 when n_1 and n_2 had standard deviation of 30, Figure 5 displays the average of all Monte-Carlo experiments for each PK parameter combination (100 pixels) excluding outliers. Figure 5 indicates that both methods provide robust estimation, except in extreme PK parameters. The large errors occur when v_e is small ($v_e = 0.01$) for K^{trans} estimation. Those areas with large correction residual errors are mainly because the curve characteristic is more sensitive to noise under those circumstances. The difference maps between the 2 correction residual error maps on the right column confirms that the inconsistency exists only under extreme situations. Both correction methods are not reliable under extreme situations. Additionally, comparison between the corrected PK
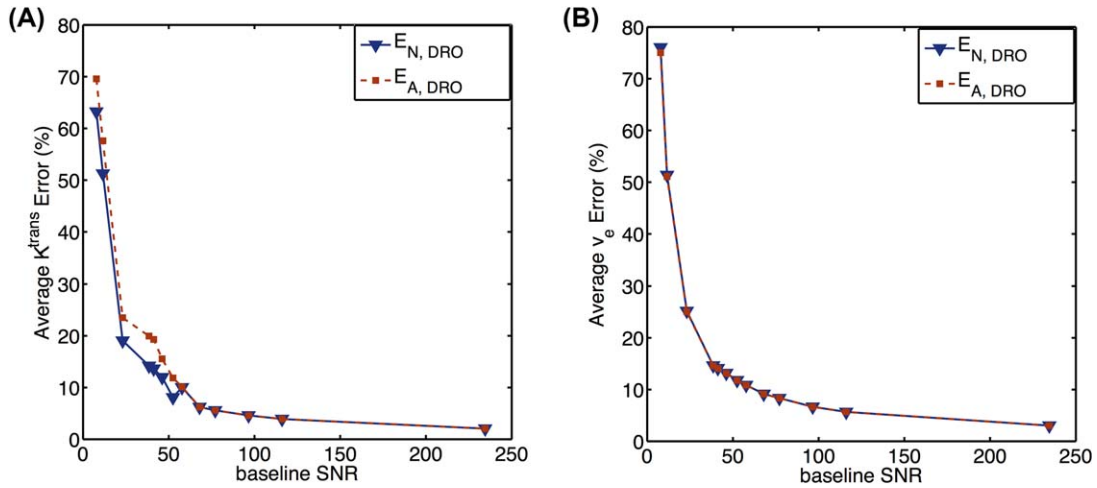
FIGURE 4 Comparison of correction residual percentage errors between 2 correction methods ($E_{N,DRO}$ and $E_{A,DRO}$) for K^{trans} maps (a) and v_e maps (b) with various levels of noise added. There are 100 Monte-Carlo simulations for each PK parameter combination. For each SNR level, noise-induced errors for 3,000 pixels ($5 \times 6 \times 100$) excluding outliers were averaged. Across all simulated baseline SNRs, the residual error for both correction methods are comparable to each other.

parameters from 2 methods, with added noise, was performed using linear regression and Bland-Altman plots (as shown in Fig. 6). With 100 times Monte-Carlo simulation for each PK parameters combination, most K^{trans} and v_e values are highly comparable between 2 methods. Pearson correlation results also show that the approximated analytical method is comparable to the conventional numerical correction methods ($r^2 = 0.97$ for K^{trans} and $r^2 = 1.00$ for v_e).

With noise added in ground truth k, the difference between average $E_{N,DRO}$ and $E_{A,DRO}$ based on the Monte-Carlo simulation over each PK parameter was smaller than 0.1%. For example, with the noise standard deviation of 0.01, both $E_{N,DRO}$ and $E_{A,DRO}$ were almost identical ($4.1 \pm 3.5\%$) for both K^{trans} and v_e. The results show that the

robustness to k measurement accuracy for those 2 correction methods is similar.

4.2 | In vivo prostate DCE-MRI data

Based on B_1^+ maps measured from 82 cases, mean k value from each subject gives a range from 0.78 to 1.22 with projected 80% intersubject B_1^+-induced error difference based on our analytical theory, indicating the necessity for B_1^+ correction.

A representative K^{trans} and v_e comparison is shown in Figure 7. This figure shows that $E_{A,in-vivo}$ (Fig. 7e,j) is small compared to $E_{B1,in-vivo}$ (Fig. 7d,i). A summary of in vivo measurements statistics for all 82 cases is shown in Table 2.
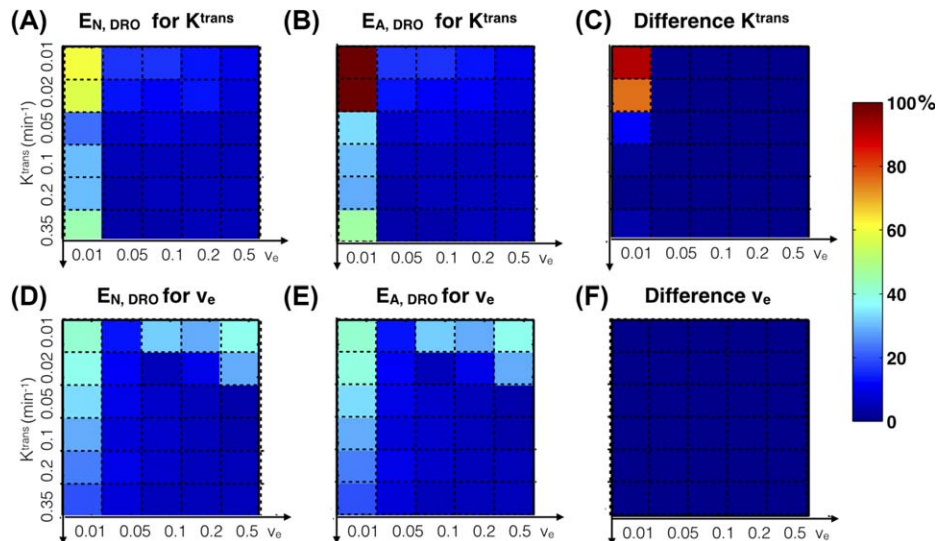
FIGURE 5 $E_{N,DRO}$ averaged for each parameter (100 pixels) (a,d) and $E_{A,DRO}$ averaged for each parameter (b,e) for K^{trans} and v_e maps with baseline SNR of 38.5. The error patterns are similar between the 2 methods. The absolute value difference maps ($E_{N,DRO} - E_{A,DRO}$) averaged for each parameter (c, f) indicate outliers appear when v_e is low, where the fitting process is more sensitive to noise.
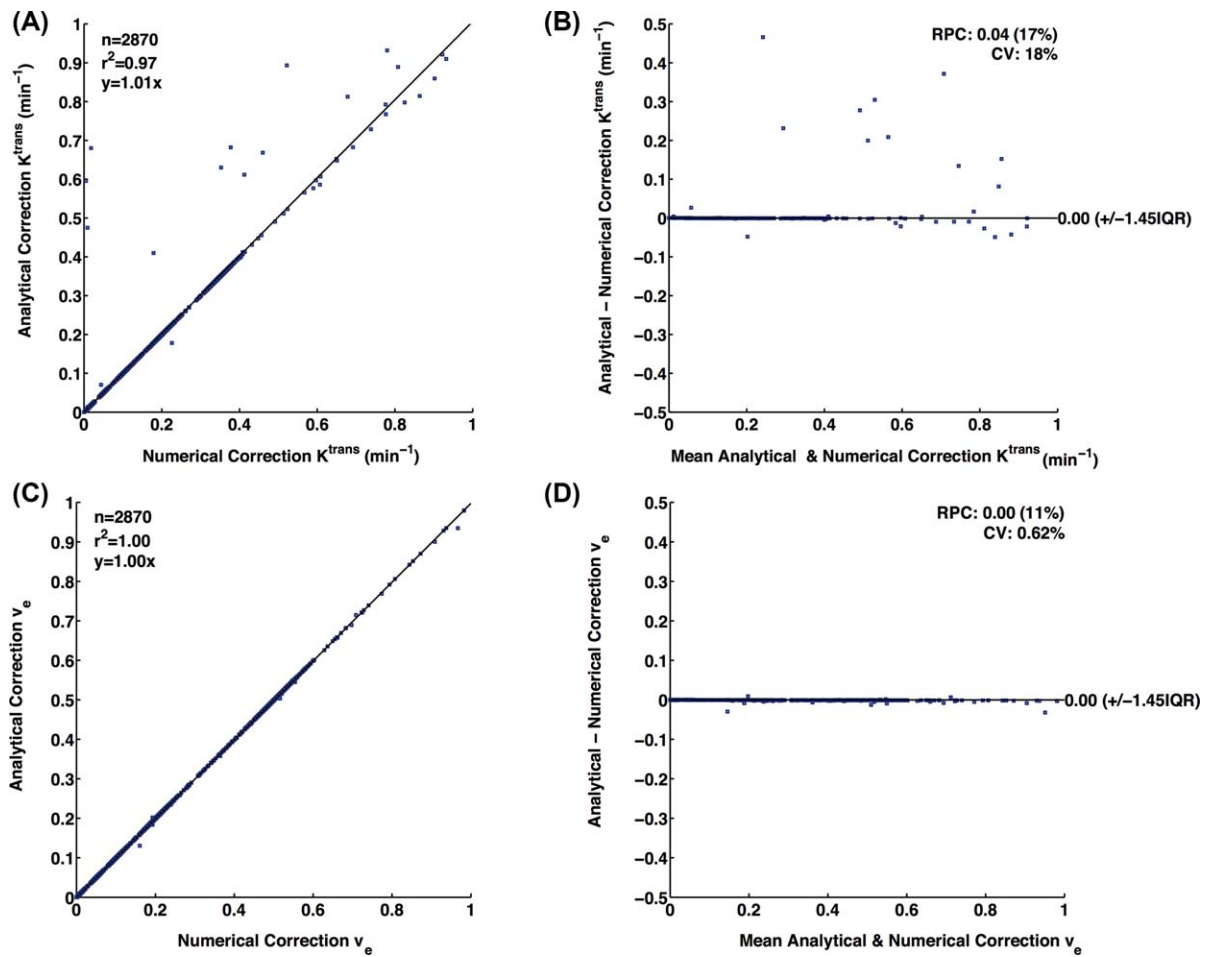
FIGURE 6 Linear regression and Bland-Altman plots for K^{trans} maps (a,b) and v_e maps (c,d) in DRO experiment with noise added. There are 100 Monte-Carlo simulations for each PK parameter combination. The corrected PK parameters from approximated analytical correction and numerical correction are highly comparable ($r^2 = 0.97$ for K^{trans} and $r^2 = 1.00$ for v_e) with baseline SNR of 38.5.

With a wide range of B_1^+ variation, residual correction errors from the analytical correction method for K^{trans} and v_e are $0.1 \pm 0.3\%$ and $0.1 \pm 0.4\%$, which are minimal. Figure 8 summarizes the average k, $E_{A,in-vivo}$ for K^{trans} and v_e among different cases, and the cases are grouped with different scanners (3T Skyra and 3T Trio). The B_1^+ inhomogeneity patterns were significantly different between 2 scanners ($P < 0.01$), attributed to different B_1^+ shimming modes. The corresponding correction residual error shows good consistency with k, and all average $E_{A,in-vivo}$ is smaller than 0.4%.

5 | DISCUSSION

In this work, a simple and practical B_1^+ correction for quantitative DCE-MRI analysis using an approximated analytical approach was proposed and evaluated. We performed a numerical simulation and a prostate DRO to evaluate the behavior of the approximated analytical method under a set of clinical imaging parameters and noise. The approximated analytical approach was also tested using 82 in vivo prostate

DCE-MRI cases by comparing it with the conventional numerical correction method. All the evaluations showed that the approximated analytical method provides comparable B_1^+ correction to the reference numerical method (less than 0.4% percentage error) under the practical situation in prostate DCE-MRI.

The approximated analytical method will enable more practical solutions for B_1^+ correction in DCE-MRI because it does not need access to the full modeling implementation in quantitative DCE-MRI analyses and does not need the acquired images for T_{10} mapping and dynamic MRI. The approximated analytical method only requires B_1^+ maps and uncorrected PK parameter maps as input to estimate the corrected PK parameters. This makes the approximated analytical correction method more practical in clinical research environments, where the model implementation access may be limited. In addition, the approximated analytical correction method provides an easy implementation of B_1^+ correction and can potentially improve the computational efficiency, because for each voxel, the calculation becomes a simple multiplication instead of a series of fitting. For
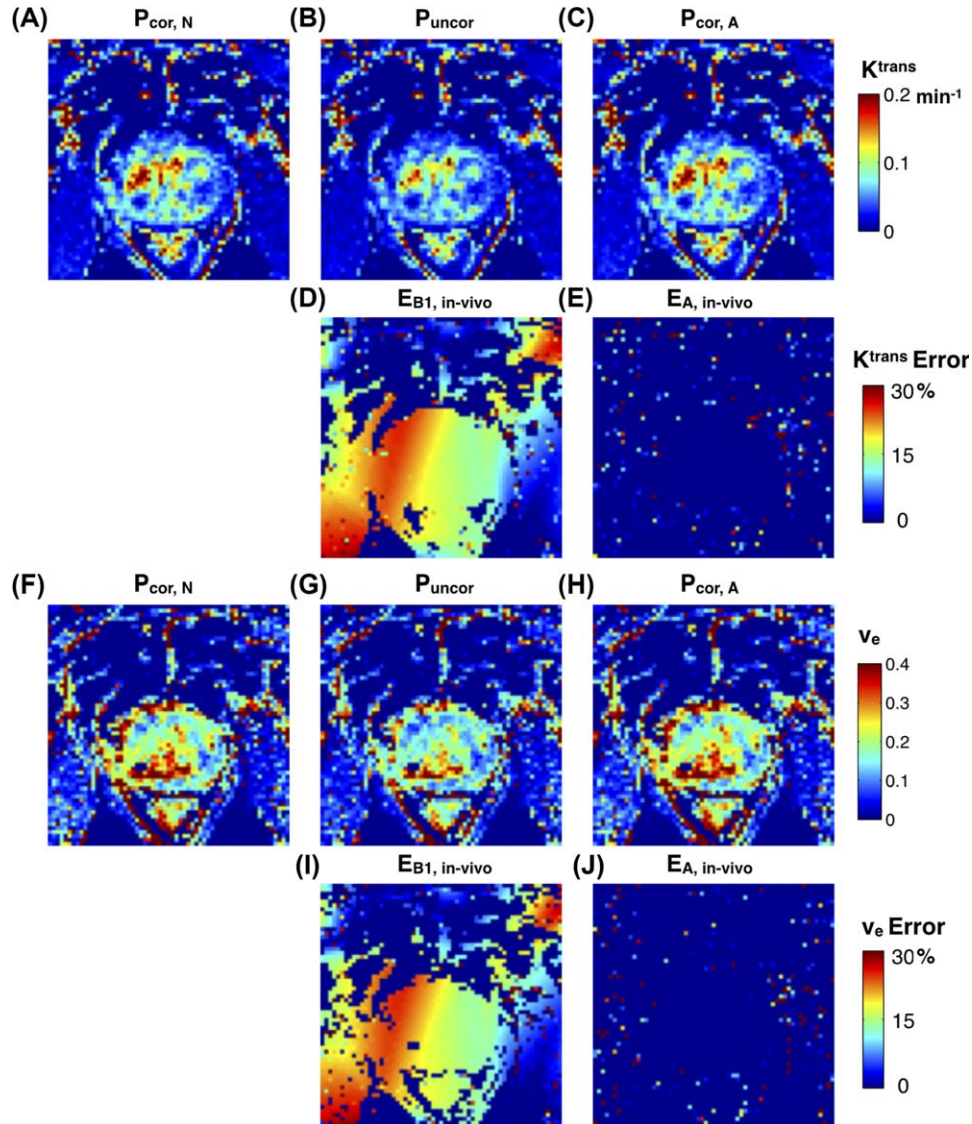
FIGURE 7 K^{trans} maps after numerical B_1^+ correction method (a), before B_1^+ correction (b) and after approximated analytical correction method (c), B_1^+ induced error for K^{trans} (d), correction residual error of K^{trans} (e), v_e maps after numerical B_1^+ correction method (f), before B_1^+ correction (g) and after approximated analytical correction method (h), B_1^+ induced error for v_e (i), and correction residual error of v_e (j)

example, in our in vivo analysis, the reference numerical correction method took more than 3 hours for each case whereas the approximated analytical correction method required less than 0.01 seconds using Matlab on the same computer.

TABLE 2 Summary of in vivo results

	Mean	Standard Deviation	95% Central Range
K^{trans} (min^{-1})	0.11	0.06	[0.03, 0.25]
v_e	0.26	0.13	[0.08, 0.60]
k	1.05	0.08	[0.83, 1.17]
$E_{A,in-vivo}$ for K^{trans} (%)	0.1	0.3	[0.0, 0.2]
$E_{A,in-vivo}$ for v_e (%)	0.1	0.4	[0.0, 0.2]

Although there exist computational acceleration techniques for the numerical correction method, such as parallelization and approximation,[38] the approximated correction method can be a good alternative when such accelerations are not available.

The approximated analytical correction relies on 3 assumptions: small flip angles, small TR/T_1, and k close to 1. The experiments in this paper use our clinical protocol to evaluate the reliability of those assumptions. The first assumption (i.e., small flip angles) can be violated with increased flip angles, and this could increase the approximation-induced error. However, in our experiment using the original QIBA DRO flip angles shown in Table 1, the maximum percentage error in the simulation is only 0.2%, which is smaller than using our protocols (maximum = 0.4%). Considering those 2 protocols are
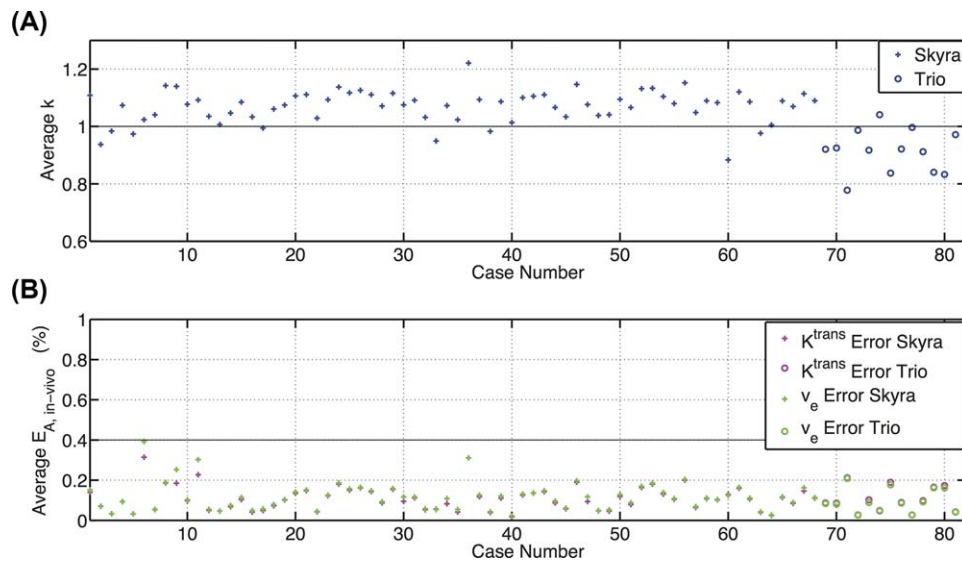
FIGURE 8 Summary of average k (a), correction residual error $E_{A,in-vivo}$ (b) for 82 patients. Different scanners (Skyra and Trio) have slightly different k distribution as shown in (a), but all the average $E_{A,in-vivo}$ is smaller than 0.4%.

similar to other studies,[7,16,39] we expect the approximated analytical correction method generalizes well to other flip angle settings. The second assumption is that k is close to 1, and based on our simulation within the k range from 0.7 to 1.3, the correction residual error is smaller than 0.4%. Even when B_1^+ overestimation is 100%, the approximation-induced error is still smaller than the baseline defined in the noise DRO experiments ($2.1 \pm 4.3\%$). Considering the increasing trend of the residual error (difference between 2 curves) shown in Figure 3, we do not expect residual error lager than 1% within a practical B_1^+ range. Also, the derivation in the Appendix actually assumes $(1-k^2) \cdot$ TR is small, considering that TR is usually a few milliseconds; the dependency on k is not strong. The last assumption is that TR/T_1 is small, and this is generally true for T_1-weighted imaging protocols. For example, in our clinical protocol, TR is 4.17 ms, and a T_1 value of $1,579 \pm 42$ ms in the prostate region was reported.[40]

Figure 4 shows how residual errors vary with baseline SNR in the DRO experiment. Because of the potential difference of our preassumed parameters in DRO compared to in vivo, the scale of signal enhancement relative to baseline signal was not exactly the same as in vivo data. Also, motion-induced errors may play a more important role than image noise for in vivo data. We do not expect that the residual error curve with baseline SNRs will be identical to in vivo data, but we believe to observe a similar trend for the residual error from the numerical correction method.

The noise in the DRO and in vivo experiments caused outliers with relatively large correction residual error when v_e was low. This is because the fitting procedure is highly sensitive to noise under those circumstances. In the DRO experiments, the numerical correction method also gives similar $E_{N,DRO}$, as shown in Figure 5. For in vivo experiments, the large

noise may arise from rectal and bowel motion. We observed outliers near the edge of the prostate as shown in Figure 2d. Although we tried to avoid the boundary of the prostate during ROI positioning, because of the anatomy complexity of in vivo cases, we still observed 0.09% of the pixels with $E_{A,in-vivo}$ lager than 1%. As shown in the DRO experiment, when large noise exists, neither of the fitting methods are reliable; therefore, in our in vivo evaluation, we reported 95% central range of the data to exclude the outliers.

In the numerical simulation and DRO experiments, we determined the percentage error relative to the ground truth, P_{nat}, to utilize the advantage of numerical simulation for error evaluation. We evaluated the percentage error relative to the numerical corrected $P_{cor,N}$ in in vivo experiments for comparison because we do not have the ground truth, and $P_{cor,N}$ is proved to be a good estimation of the ground truth in simulation experiment in noise-free situation ($E_{N,DRO}$ less than 0.2%). With this in mind, we chose $P_{cor,N}$ as the reference in in vivo experiments because we want the evaluation in in vivo experiment be more consistent with that of the simulation and DRO experiments. However, the DRO experiment also showed that if noise is present, $P_{cor,N}$ might deviate from the ground truth (as shown in Fig. 5a). With baseline SNR of 38.5 and without taking outliers into evaluation, the numerical correction method will have an average of 14.4% $E_{N,DRO}$. This error will lead to inconsistent evaluation between the results of simulation and in vivo experiments.

Our study included a few limitations. One limitation is that the practical utility of the approximated correction is mainly limited to situations where closed-form or commercial software is used for quantitative DCE-MRI analysis. However, closed or commercial software is widely used in clinical prostate DCE-MRI,[41] and, to the best of our knowledge, most of them do not include the B_1^+ correction. Also, our approach

can be practically useful when an in-house B_1^+ correction process is time-consuming, especially in clinical or clinical research settings. The second limitation is that we focused on the error propagation behavior under the standard Tofts model with population-averaged AIFs, which are commonly used techniques in clinical prostate DCE-MRI.[7,32] The error propagation analysis may need to be updated if other PK modeling settings are used for DCE-MRI quantification, including subject-based measured AIF[42] and/or the extended Tofts model.[25] For a subject-based measured AIF, our approximation method can be easily modified with minimal error if blood T_{10} is also measured (AIF1). The modified correction method becomes $\frac{K^{trans}{}_I}{K^{trans}} \approx \left(\frac{k_t}{k_p}\right)^2$, $\frac{v_e{}_I}{v_e} \approx \left(\frac{k_t}{k_p}\right)^2$, where k_t and k_p are k values in measured blood and tissue pixel or ROI. However, if predetermined blood T_{10} is used for the subject-based measured AIF (AIF2), the modification becomes highly complicated, which may need to be further investigated in future. With DRO simulation with $k_t = 1.2$ and $k_p = 1.1$, $E_{A,DRO}$ using AIF1 is 0.4% for K^{trans} whereas $E_{A,DRO}$ using AIF2 is 87.6% for K^{trans}. Last, the difference between the standard and extended Tofts models is generally small in the prostate attributed to the small contribution of v_p. Based on the in vivo simulation (n = 82), v_p within the prostate was 0.0026 ± 0.0030, and the approximation errors with the extended Tofts model ($E_{A,in-vivo}$) were $0.1 \pm 0.1\%$ and $0.1 \pm 0.6\%$ for K^{trans} and v_e, similar to the ones with the standard Toft model. With higher v_p relative to v_e, the approximation-induced error could be significant, and therefore the method is limited to organs with small v_p (see Supporting Information Figure S2 for the influence of v_p in the extended Tofts model).

6 | CONCLUSION

We have demonstrated the feasibility and accuracy of a simple approximated analytical B_1^+ correction approach for quantitative prostate DCE-MRI. This method only requires B_1^+ maps and uncorrected PK parameters as input to calculate corrected PK parameter maps. The approximated analytical method was evaluated by both numerical digital reference object and 82 in vivo prostate DCE-MRI cases. In all cases, the approximated analytical method had very low approximation error (less than 0.3% correction residual error compared to conventional numerical correction within 95% central range). Most important, this B_1^+ correction method can be easily implemented in clinical workflow, and has the potential to improve the performance and reproducibility of clinical quantitative prostate DCE-MRI.

ORCID

Holden H. Wu http://orcid.org/0000-0002-2585-5916

REFERENCES

[1] Siegel RL, Miller KD, Jemal A. Cancer statistics, 2016. *CA Cancer J Clin* 2016;66:7–30.

[2] Litjens G, Debats O, Barentsz J, Karssemeijer N, Huisman H. Computer-aided detection of prostate cancer in MRI. *IEEE transactions on medical imaging.* 2014;33:1083–1092.

[3] Isebaert S, De Keyzer F, Haustermans K, et al. Evaluation of semi-quantitative dynamic contrast-enhanced MRI parameters for prostate cancer in correlation to whole-mount histopathology. *Eur J Radiol* 2012;81:e217–e222.

[4] Alonzi R, Padhani AR, Allen C. Dynamic contrast enhanced MRI in prostate cancer. *Eur J Radiol* 2007;63:335–350.

[5] Kamrava M, Kishan AU, Margolis DJ, et al. Multiparametric magnetic resonance imaging for prostate cancer improves Gleason score assessment in favorable risk prostate cancer. *Pract Radiat Oncol* 2015;5:411–416.

[6] Khalifa F, Soliman A, El-Baz A, et al. Models and methods for analyzing DCE-MRI: a review. *Med Phys* 2014;41:124301.

[7] Franiel T, Hamm B, Hricak H. Dynamic contrast-enhanced magnetic resonance imaging and pharmacokinetic models in prostate cancer. *Eur Radiol* 2011;21:616–626.

[8] Vos EK, Litjens GJ, Kobus T, et al. Assessment of prostate cancer aggressiveness using dynamic contrast-enhanced magnetic resonance imaging at 3 T. *Eur Urol* 2013;64:448–455.

[9] Fennessy FM, McKay RR, Beard CJ, Taplin ME, Tempany CM. Dynamic contrast-enhanced magnetic resonance imaging in prostate cancer clinical trials: potential roles and possible pitfalls. *Transl Oncol* 2014;7:120–129.

[10] Tofts P. T1-weighted DCE imaging concepts: modelling, acquisition and analysis. *Signal* 2010;500:400.

[11] Gupta RK. A new look at the method of variable nutation angle for the measurement of spin-lattice relaxation times using fourier transform NMR. *J Magn Reson* 1977;25:231–235.

[12] Homer J, Beevers MS. Driven-equilibrium single-pulse observation of T1 relaxation. A reevaluation of a rapid "new" method for determining NMR spin-lattice relaxation times. *J Magn Reson* 1985;63:287–297.

[13] Treier R, Steingoetter A, Fried M, Schwizer W, Boesiger P. Optimized and combined T1 and B1 mapping technique for fast and accurateT1 quantification in contrast-enhanced abdominal MRI. *Magn Reson Med* 2007;57:568–576.

[14] Tsai WC, Kao KJ, Chang KM, et al. B1 field correction of T1 estimation should be considered for breast dynamic contrast-enhanced MR imaging even at 1.5 T. *Radiology* 2017;282:55–62.

[15] Subashi E, Choudhury KR, Johnson GA. An analysis of the uncertainty and bias in DCE-MRI measurements using the spoiled gradient-recalled echo pulse sequence. *Med Phys* 2014;41:032301.

[16] Ocak I, Bernardo M, Metzger G, et al. Dynamic contrast-enhanced MRI of prostate cancer at 3 T: a study of pharmacokinetic parameters. *Am J Roentgenol* 2007;189:W192–W201.

[17] Soher BJ, Dale BM, Merkle EM. A review of MR physics: 3T versus 1.5T. *Magn Reson Imaging Clin N Am* 2007;15:277–290.

[18] Rangwala NA, Dregely I, Wu HH, Sung K. Optimization and evaluation of reference region variable flip angle (RR-VFA) B1 + and T 1 mapping in the prostate at 3T. *J Magn Reson Imaging* 2017;45:751–760.

[19] Di Giovanni P, Azlan CA, Ahearn TS, Semple SI, Gilbert FJ, Redpath TW. The accuracy of pharmacokinetic parameter measurement in DCE-MRI of the breast at 3 T. *Phys Med Biol* 2010; 55:121–132.

[20] Cunningham CH, Pauly JM, Nayak KS. Saturated double-angle method for rapid B1 + mapping. *Magn Reson Med* 2006;55: 1326–1333.

[21] Sacolick LI, Wiesinger F, Hancu I, Vogel MW. B 1 mapping by Bloch-Siegert shift. *Magn Reson Med* 2010;63:1315–1322.

[22] Yarnykh VL. Actual flip-angle imaging in the pulsed steady state: a method for rapid three-dimensional mapping of the transmitted radiofrequency field. *Magn Reson Med* 2007;57:192–200.

[23] Sung K, Saranathan M, Daniel BL, Hargreaves BA. Simultaneous T 1 and B 1 + mapping using reference region variable flip angle imaging. *Magn Reson Med* 2013;70:954–961.

[24] Bedair R, Graves MJ, Patterson AJ, et al. Effect of radiofrequency transmit field correction on quantitative dynamic contrast-enhanced MR imaging of the breast at 3.0 T. *Radiology* 2016;279:368–377.

[25] Tofts PS. Modeling tracer kinetics in dynamic Gd-DTPA MR imaging. *J Magn Reson Imaging* 1997;7:91–101.

[26] Zhong X, Rangwala N, Raman S, Margolis D, Wu H, Sung K. B1 + inhomogeneity correction for estimation of pharmacokinetic parameters through an approximation approach. In Proceedings of the 24th Annual Meeting of ISMRM, 2016, Singapore. p. 2491.

[27] Bosca RJ, Jackson EF. Creating an anthropomorphic digital MR phantom—an extensible tool for comparing and evaluating quantitative imaging algorithms. *Phys Med Biol* 2016;61:974–982.

[28] Mehrtash A, Gupta SN, Shanbhag D, et al. Bolus arrival time and its effect on tissue characterization with dynamic contrast-enhanced magnetic resonance imaging. *J Med Imaging* 2016;3:14503.

[29] Zhong X, Wu H, Nayak K, Sung K. Evaluation of approximation method for B1 + correction using digital reference object in prostate DCE-MRI. In Proceedings of the 25th Annual Meeting of ISMRM, 2017, Honolulu, HI. p. 622.

[30] Coleman TF, Li Y. An interior trust region approach for nonlinear minimization subject to bounds. *SIAM J Optim* 1996;6:418–445.

[31] QIBA Content. Daniel P. Barboriak Lab. https://sites.duke.edu/dblab/qibacontent/. 2012. Accessed June 8, 2016.

[32] Azahaf M, Haberley M, Betrouni N, et al. Impact of arterial input function selection on the accuracy of dynamic contrast-enhanced MRI quantitative analysis for the diagnosis of clinically significant prostate cancer. *J Magn Reson Imaging* 2016;43:737–749.

[33] Parker GJ, Roberts C, Macdonald A, et al. Experimentally-derived functional form for a population-averaged high-temporal-resolution arterial input function for dynamic contrast-enhanced MRI. *Magn Reson Med* 2006;56:993–1000.

[34] Weinmann HJ, Laniado M, Mützel W. Pharmacokinetics of GdDTPA/dimeglumine after intravenous injection into healthy volunteers. *Physiol Chem Phys Medical NMR* 1984;16:167–172.

[35] Fritz-Hansen T, Rostrup E, Larsson HB, et al. Measurement of the arterial concentration of Gd-DTPA using MRI: a step toward quantitative perfusion imaging. *Magn Reson Med* 1996;36:225–231.

[36] Peng Y, Jiang Y, Yang C, et al. Quantitative analysis of multiparametric prostate MR images: differentiation between prostate cancer and normal tissue and correlation with gleason score—a computer-aided diagnosis development study. *Radiology* 2013; 267:787–796.

[37] Ma J. Breath-hold water and fat imaging using a dual-echo two-point dixon technique with an efficient and robust phase-correction algorithm. *Magn Reson Med* 2004;52:415–419.

[38] Orton MR, D'Arcy JA, Walker-Samuel S, et al. Computationally efficient vascular input function models for quantitative kinetic modelling using DCE-MRI. *Phys Med Biol* 2008;53:1225–1239.

[39] Portalez D, Mozer P, Cornud F, et al. Validation of the European Society of Urogenital Radiology scoring system for prostate cancer diagnosis on multiparametric magnetic resonance imaging in a cohort of repeat biopsy patients. *Eur Urol* 2012;62:986–996.

[40] de Bazelaire CMJ, Duhamel GD, Rofsky NM, Alsop DC. MR imaging relaxation times of abdominal and pelvic tissues measured in vivo at 3.0 T: preliminary results. *Radiology* 2004;230: 652–659.

[41] Chao SL, Metens T, Lemort M. TumourMetrics: a comprehensive clinical solution for the standardization of DCE-MRI analysis in research and routine use. *Quant Imaging Med Surg* 2017; 7:1–15.

[42] Port RE, Knopp MV, Brix G. Dynamic contrast-enhanced MRI using Gd-DTPA: interindividual variability of the arterial input function and consequences for the assessment of kinetics in tumors. *Magn Reson Med* 2001;45:1030–1038.

[43] Tofts PS, Kermode AG. Measurement of the blood-brain barrier permeability and leakage space using dynamic MR imaging. 1. Fundamental concepts. *Magn Reson Med* 1991;17:357–367.

SUPPORTING INFORMATION

Additional Supporting Information may be found in the online version of this article.

FIGURE S1. $E_{A, DRO}$ maps using 3 population-averaged AIFs for K^{trans} estimation (a–c) and for v_e estimation (d–f). The maximum residual error for K^{trans} is 0.2% and for v_e is 0.4%.
FIGURE S2. Extended Tofts model was simulated in the DRO with 3 v_p values, 0.001, 0.005, and 0.01. The results were evaluated using $E_{A,DRO}$ for K^{trans} (a–c) and v_e estimation (d–f).

APPENDIX

In the VFA process, the fitting procedure is simplified to only 2 flip angles α_1 and α_2. The measured signals with the 2 flip angles S_1 and S_2 are given as constant, namely $S_1 = S_1'$ and $S_2 = S_2'$. Based on Equation 1, in an actual situation, $S_i = \frac{M_0(1-E'_{10})sink\alpha_i}{1-E'_{10}cosk\alpha_i}$ for both signals S_1 and S_2.

First, we want to find the relationship between corrected E_{10}' and uncorrected E_{10}. The corrected E_{10}' can be expressed as a function of uncorrected E_{10} as follows (Eq. A1):

$$E_{10} = \frac{\dfrac{S_2}{sin\alpha_2} - \dfrac{S_1}{sin\alpha_1}}{\dfrac{S_2}{tan\alpha_2} - \dfrac{S_1}{tan\alpha_1}}$$

$$= \frac{(1-E'_{10}cosk\alpha_1)sink\alpha_2 sink\alpha_1 - (1-E'_{10}cosk\alpha_2)sink\alpha_1 sink\alpha_2}{(1-E'_{10}cosk\alpha_1)sink\alpha_2 sink\alpha_1 cosk\alpha_2 - (1-E'_{10}cosk\alpha_2)sink\alpha_1 sink\alpha_2 cosk\alpha_1}$$

(A1)

Equation A1 is the analytical form of the linear regression using 2 flip angles. When using more than 2 flip angles, the fitting estimation will be the same using any 2 flip angles without noise because it is an overdetermined problem.

With the assumptions that flip angles α_i in rad are close to zero ($\alpha_i^3 \approx 0$), based on Taylor Series, we could get that $sin\alpha_i \approx \alpha_i$, $cos\alpha_i \approx 1 - \frac{\alpha_i^2}{2}$ for both flip angles α_1 and α_2. By substitute those equations into Equation A1, we could get a simplified version of the relationship (Eq. A2).

$$E_{10} \approx 1 - \frac{1-E_{10}'}{1-E'_{10}+k^2 E_{10}'}$$

(A2)

Then, based on the assumption that $\frac{TR}{T_1} \approx 0$ and Taylor Series $\ln(x) \approx x - 1$, it can be derived that $E_{10} \approx 1 - \frac{TR}{T_{10}}$ and $E_{10}' \approx 1 - \frac{TR}{T_{10}'}$. By substituting these equations into Equation A2, we could get the relationship between corrected T_{10}' and uncorrected T_{10} (Eq. A3).

$$T_{10} \approx (1-k^2)TR + k^2 T_{10}'$$

(A3)

With a small TR (0.004 seconds in our protocol) and k close to 1, the first term on the right side of Equation (A3) is close to zero. The relationship can be further simplified as (Eq. A4).

$$\frac{T_{10}'}{T_{10}} \approx \frac{1}{k^2}$$

(A4)

In the process of dynamic T_1 quantification, based on $\frac{S(t)}{S_0} = \frac{\left(1-E_1(t)\right)(1-E_{10}cos\beta)}{(1-E_{10})\left(1-E_1(t)cos\beta\right)}$, $T_1(t)$ at each time point is calculated from T_{10} and the ratio between signal at baseline S_0 and signal at the corresponding time point $S(t)$. In this process, the ratios between signals are given as constant, as expressed in (Eq. A5):

$$\frac{S'(t)}{S_0'} = \frac{S(t)}{S_0}.$$

(A5)

After substituting Equation 1 into Equation A5 for all four signals and reformatting, we could get the following equation (Eq. A6):

$$\frac{[1-E_1(t)][1-E_1'(t)cosk\beta]}{[1-E_1'(t)][1-E_1(t)cos\beta]} = \frac{[1-E_{10}][1-E'_{10}cosk\beta]}{[1-E_{10}'][1-E_{10}cos\beta]}$$

(A6)

Based on the similar assumptions of small flip angle β, we could get $sin\beta \approx \beta$, $cos\beta \approx 1 - \frac{\beta^2}{2}$. By substituting those equations and Equation A2 into Equationn A6, we could prove that (Eq. A7):

$$\frac{[1-E_1(t)][1-E_1'(t)cosk\beta]}{[1-E_1'(t)][1-E_1(t)cos\beta]} \approx 1$$

(A7)

Then, similarly, based on assumption of $\frac{TR}{T_1(t)} \approx 0$ and $\beta \approx 0$, Equation A7 could be further simplified as (Eq. A8):

$$E_1(t) \approx 1 - \frac{1-E_1'(t)}{1-E_1'(t)+k^2 E_1'(t)}$$

(A8)

We can find the similarity between Equations A8 and A2. Correspondingly, as shown in Equation A4, with assumptions of small TR and k^2 close to 1, we could further simplify Equation A8 to the following equation (Eq. A9):

$$\frac{T_1'(t)}{T_1(t)} \approx \frac{1}{k^2}.$$

(A9)

Now we got the relationship of corrected and uncorrected T_1 values before and after contrast agent, and from the linearity of contrast agent shown in Equation 4, it could be easily derived that the relationship between corrected and uncorrected tissue contrast agent concentration $C_t'(t)$ and $C_t(t)$ is as follows (Eq. A10):

$$\frac{C_t'(t)}{C_t(t)} \approx k^2$$

(A10)

As the last step, according to Equation 5 of the standard Tofts model,[43] with a fixed $C_p(t)$ which is not influenced by B_1^+, the ratio between uncorrected and corrected K^{trans} is equal to the ratio of tissue contrast agent concentration (Eq. A11).

$$\frac{K^{trans'}}{K^{trans}} = \frac{C_t'(t)}{C_t(t)} \approx k^2$$

(A11)

Because the integration following K^{trans} in Tofts model is not related to B_1^+, namely $\frac{K^{trans'}}{v_e'} = \frac{K^{trans}}{v_e}$, the ratio between v_e would be (Eq. A12):

$$\frac{v_e'}{v_e} = \frac{K^{trans'}}{K^{trans}} \approx k^2$$

(A12)

In summary, based on 3 basic assumptions during the whole acquisition process: (1) small flip angle, (2) small TR and T_1 ratio, and (3) k is close to 1, under the standard Tofts model and a population-averaged AIF condition, relationships between corrected and uncorrected PK parameters can be simplified to $\frac{K^{trans'}}{K^{trans}} \approx k^2$, $\frac{v_e'}{v_e} \approx k^2$.